Research Paper

Fault detection and isolation for a secondary loop refrigeration system

Agnes Poks [*], Markus Fallmann, Lorenz Fink, Lukas Rinnofner, Martin Kozek

Vienna University of Technology, Institute of Mechanics and Mechatronics, Division of Control and Process Automation, Getreidemarkt 9, 1060 Vienna, Austria

ARTICLE INFO

ABSTRACT

Secondary loop refrigeration systems offer advantages over conventional system architectures: refrigerant charge reduction, maintenance simplification, and reduced safety hazards. Currently, no model-based fault detection for a secondary loop system has been reported. This article presents a fault detection and isolation scheme for a secondary loop refrigeration system where parametric faults (dirt/ice-buildup and secondary loop pump failure) and sensor faults (four temperature sensors in the secondary loop) are detected and isolated. The fault detection and isolation system is based on unknown input observers and on extended Kalman filters. The models are obtained through physical relations combined with experimental parameter determination (gray-box model) and are cross-validated against measurement data. The complete fault detection and isolation architecture is experimentally validated on a secondary loop refrigeration system mounted on a cooling box inside a climate chamber. Experimental results show that important parametric faults can be reliably detected and isolated, and the fault detection and isolation of sensor faults are effective.

1. Introduction

Refrigeration systems (RS) are in ever-increasing use throughout the world [1,2]. One means of facilitating condition-driven maintenance is the implementation of a fault detection and isolation (FDI) method in these systems. The general advantages of an FDI system are reduced electricity and maintenance costs, reduced loss of goods, and reduced carbon emissions [3]. Potential energy savings from FDI in building systems and equipment are estimated to be 5% to 15% [4]. FDI enables the detection and correct interpretation of irregular operation, which can be caused by an actuator or sensor failure, or by parametric faults such as icing or fouling of heat exchangers [5,6].

Existing FDI methods can be classified into knowledge-based and data-driven methods [7,8] as well as model-based methods. Knowledge-based methods are mostly qualitative and require deep knowledge of the specific process [9]. New data-driven approaches have similar accuracy to model-based methods, although a major disadvantage of data-driven methods is that they require suitable data and are sensitive to pattern changes [10]. A review of FDI in building heating, ventilation, and air-conditioning as well as refrigeration using feature engineering is given in [11], where it is stated that in some practical cases, it is difficult to obtain sufficient fault data and labels. Moreover, due to potentially large computational costs, future FDI systems should be executed using cloud computing. In [12], an overview of FDI applied to supermarket refrigeration concludes that the mostly data-driven methods applied to this area along with secondary loops may complicate the application of model-based methods.

Model-based methods require knowledge of the underlying system physics together with a suitable method to fit parameters. A number of model-based methods based on observer design are presented in [13]. In [14], FDI is investigated using a bank of unknown input observers (UIO) for a supermarket refrigeration system. In the second publication, [15] FDI adding the Kalman filter (KF) technique to the same system is explored. The simulation results show that the EKF-based FDI method generally performs better and faster than the KF-based method. The nonlinear model utilized in these publications is derived and presented in [16]. Both papers only cover conventional RSs, and secondary loop faults are not discussed.

Similar FDI approaches for different applications have been published previously. In [17], the problem of fault diagnosis in a three-tank hydraulic system is presented. UIO and extended Kalman filters (EKF) are used to detect and isolate actuator and sensor faults, although no experimental results are shown. In [18], a parity equation, an observer, and a KF for a linearized system are applied. Three different residuals are compared, focusing on the sensor faults of the thermal management system. Although a real driving cycle is used, no nonlinear observer is employed and only sensor faults are covered. A method suitable for strongly nonlinear processes is presented in [19], where a design method for a nonlinear unknown input observer is presented. The proposed method is based on cubature rules to simplify calculations. It is applied to a continuously stirred tank reactor, and only sensor faults are considered. An observer-based FDI method for a single loop RS

Nomenclature

Mathematical notation and accents

$\mathbb{N}$	Natural numbers
$\mathbb{R}$	Real numbers
$\mathcal{N}$	Gaussian distribution
rank $[\boldsymbol{X}]$	Rank of matrix $\boldsymbol{X}$
$\dot{x}$	Time derivative of x (continuous time system)
$\boldsymbol{x}^{\mathrm{T}}$	Transpose of $\boldsymbol{x}$
$\boldsymbol{X}^{-1}$	Inverse of matrix $\boldsymbol{X}$
$\boldsymbol{x}^{-}$	Prediction of x
$\hat{x}$	Correction/estimate of x
x^{*}	Optimized value of x
$\bar{x}$	Mean of x

Latin letters

$\boldsymbol{A}$	System matrix
$\boldsymbol{B}$	Input matrix
$\boldsymbol{C}$	Output matrix
$\boldsymbol{c}$	Output vector
c_p	Specific heat capacity
f	System equation
h	Output equation
l	Number of sensor faults
j	Number of parametric faults
J	Objective function
$\dot{m}$	Mass flow
$\boldsymbol{K}_{\mathrm{ekf}}$	EKF-gain matrix
$\boldsymbol{K}_{\mathrm{uio}}$	UIO-gain matrix
δ	Threshold FDI
$\boldsymbol{P}$	Covariance matrix of estimation error
Q	Variance of process noise
$\boldsymbol{Q}$	Covariance matrix of process noise isolation
$\dot{Q}$	Heat flow
r	Residual
R	Variance of measurement noise
$\boldsymbol{P}$	Covariance matrix of estimation error
$\mathcal{F}$	Fault detection variable
m	Mass KF Kalman filter
n	Rotational speed
$\boldsymbol{u}$	Input vector
υ	Measurement noise
w	Process noise
$\boldsymbol{w}$	Vector of process noise
x	State
$\boldsymbol{x}$	State vector
y	Output
z	UIO state

Greek letters

α	Heat transition coefficient
β	Wall model coefficient
γ	Pump mass flow
ζ	Pump power
Δ	Difference
ε	Vector of estimation error
ϑ	Temperature
θ	Parameter vector of physical model
κ	Gain factor model
ϕ	Threshold function coefficients

Subscripts and superscripts

icb	Isolated cooling box
k	Discrete time
d	Detection
fan	Air chiller fan
air	Air flow
gly	Glycol
eva	Evaporator
amb	Ambient
ice	Icing-fault
in	In-flowing position
ref	Reference
cpr	Compressor
pump	Glycol–water pump
out	Out-flowing position
s	Sensor fault
p	Parametric fault
wait	Holding time detection
hold	Holding time isolation

Acronyms

NTU	Number of Transfer
EKF	Extended Kalman filter
KF	Kalman filter
UIO	Unknown Input Observer
FDI	Fault Detection Isolation
RS	Refrigeration system
ICB	Isolated cooling box
RMSE	Root-mean-square error
NRMSE	Normalized root mean square error
COP	Coefficient of performance
MPC	Model predictive control
PT1	Proportional transfer function
PI	Proportional Integral

in an automotive air-conditioning system is presented in [20]. Sensor, actuator, as well as parametric faults, are detected using dedicated H_{∞} filters based on linear models of the system. Experimental results show the effectiveness of the approach.

Secondary loop systems have evolved in the search for more energy-efficient refrigeration systems [21]. The paper [22] presents a comprehensive review of secondary loop refrigeration systems. The secondary loop is isolated from the primary loop, which brings many benefits in refrigerant charge reduction, leakage reduction, and maintenance simplification compared to conventional refrigeration systems [23]. According to the analyses in [24] secondary loop refrigeration systems show improved annual coefficient of performance (COP) values compared to standard single loop systems. In [25] the combination of a carbon dioxide process with a secondary loop shows advantages in COP and total electrical energy consumption.

While secondary loop RSs show many advantages in handling and efficiency, the design of an FDI system is still at the development stage; due to the complications of additional components and their interaction, in-depth investigations on a suitable FDI system are called for.

The aim of this study is to provide the design of an FDI system for a small secondary loop RS and to demonstrate its performance
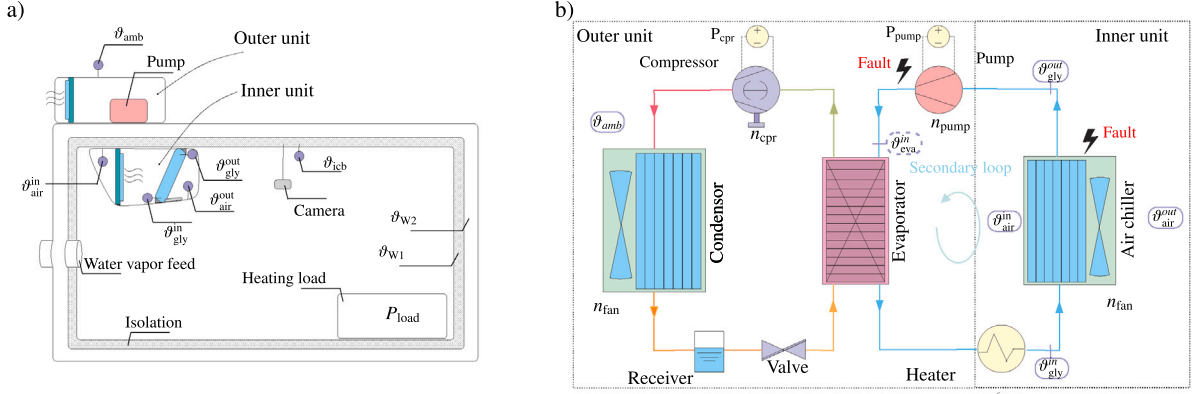
Fig. 1. (a) Schematic diagram for the secondary loop of the refrigeration system in the experimental setup. (b) Sketch of the cooling system test bench in a climate chamber.

on an experimental test bench. The methods used include analytical modeling of the system, parameter estimation and model validation using measured data, model-based state estimation using UIO and EKF, and a hierarchical fault identification logic.

The main contributions of this study are as follows:

- A simple yet accurate dynamic model of the secondary loop RS is built from non-stationary energy balances and regression models for state estimation. Existing models for simulation purposes are too complex for this task.
- It is shown that the model parameters can be optimized using a brief set of measured data.
- The observer structure and the fault identification logic are tailored to identify both sensor faults and the parametric faults for the secondary loop pump and icing.
- A systematic way to select the threshold values of the fault identification logic is presented.
- In contrast to [14,15], both Monte Carlo simulations and experimental results demonstrate the functionality and performance of the presented approach.

Note that the presented FDI method cannot isolate simultaneous faults, although a more complex observer structure could in principle fulfill this task [11].

The remainder of this paper is structured as follows: In Section 2 the models of the secondary loop refrigeration system (RS) and insulated cooling box (ICB) are presented. Section 3 describes the model equations. The parametrization of the developed model and its validation based on measurements is detailed in Section 4. The structure consisting of the EKF and UIO is presented in Section 5. Furthermore, the logic and the model-based FDI approach are explained. Section 6 shows the laboratory setup of the test bench where the FDI algorithm was experimentally validated followed by the description of the fault conditions in Section 7. In Section 8, the applied FDI approach and experimental results are presented. The findings are outlined in the Conclusion.

2. System description

The proposed approach is implemented on a test bench with a secondary loop RS fixed to an insulated cooling chamber. Fig. 1 shows the test bench located in a temperature-controlled chamber with circulating airflow and stable ambient temperature.

In subplot (a) of Fig. 1 the cooling system consists of an outer and an inner unit. In the outer unit, as also visible in subplot (b) of Fig. 1, the condenser is integrated. Outside of the outer unit, a sensor measuring the ambient temperature $\vartheta_{amb} \in \mathbb{R}$ is mounted.

Inside the outer unit, the glycol pump is located. The wooden box is insulated with extruded styrofoam and with a size of 1.78 m x 1.72 m x

1.09 m has similar dimensions and thermal characteristics as the cool box of a delivery vehicle [26]. The refrigeration loop consists of a condenser, an evaporator, a thermostatic expansion valve, and a compressor. The secondary loop consists of a water pump, a heater, and an air chiller as shown in Fig. 1(b).

The air chiller inside the box is equipped with a flap, partly covering the air path of the chiller when closed.

The sensors for the glycol temperature ϑ_{gly}^{in} and $\vartheta_{gly}^{out} \in \mathbb{R}$ are located in the inner unit near the air-chiller, as shown in Fig. 1(a). The sensors for the air-flow temperature ϑ_{air}^{in} and $\vartheta_{air}^{out} \in \mathbb{R}$ are located in front of and behind the air-chiller.

A heating load $P_{load} \in \mathbb{R}_{\geq 0}$ is placed inside the box to emulate time-varying heat loads such as ambient temperature or irradiation. Additionally, an electrically heated pot can be controlled, where boiling water generates high humidity to emulate the effect of door openings in humid ambient air conditions.

The complete data acquisition system is presented in detail in [27].

3. System model

In this section, the mathematical model of the RS with secondary loop is described. It forms the base of the observer designs in the later sections. The model is based on [26,28] and [29] with some adaptions for the secondary loop system.

3.1. Model formulation

The system shown in Fig. 1 is characterized by seven non-stationary energy balances:

$$\frac{d\vartheta_{gly}^{in}}{dt} = \frac{\kappa_1}{\tau_1}\left(\frac{-\dot{Q}_{eva}}{\dot{m}_{gly}c_{p,gly}} + \vartheta_{eva}^{in}\right) - \frac{\vartheta_{gly}^{in}}{\tau_1} \tag{1}$$

$$\frac{d\vartheta_{gly}^{out}}{dt} = \frac{\kappa_2}{\tau_2}\left(\frac{\dot{Q}_0}{\dot{m}_{gly}c_{p,gly}} + \vartheta_{gly}^{in}\right) - \frac{\vartheta_{gly}^{out}}{\tau_2} \tag{2}$$

$$\frac{d\vartheta_{air}^{in}}{dt} = \frac{\kappa_3}{\tau_3}\vartheta_{icb} - \frac{\vartheta_{air}^{in}}{\tau_3} \tag{3}$$

$$\frac{d\vartheta_{air}^{out}}{dt} = \frac{\kappa_4}{\tau_4}\left(\frac{\dot{Q}_0}{\dot{m}_{air}c_{p,air}} + \vartheta_{icb}\right) - \frac{\vartheta_{air}^{out}}{\tau_4} \tag{4}$$

$$\frac{d\vartheta_{icb}}{dt} = -\frac{\dot{Q}_0}{m_{air}c_{p,air}} + \frac{\alpha A_{icb}}{m_{air}c_{p,air}}\left(\vartheta_{W1} - \vartheta_{icb}\right) - \frac{P_{load}}{m_{air}c_{p,air}} \tag{5}$$

$$\frac{d\vartheta_{W1}}{dt} = \beta_1\left(\vartheta_{W1} - \vartheta_{icb}\right) + \beta_2\left(\vartheta_{W2} - \vartheta_{W1}\right) \tag{6}$$

$$\frac{d\vartheta_{W2}}{dt} = \beta_3\left(\vartheta_{W2} - \vartheta_{W1}\right) + \beta_4\left(\vartheta_{amb} - \vartheta_{W2}\right) \tag{7}$$

The states are $\vartheta_{gly}^{in}, \vartheta_{gly}^{out}$ in the water–glycol fluid, the air temperatures before and after the air chiller ϑ_{air}^{in} and ϑ_{air}^{out}, $\vartheta_{icb} \in \mathbb{R}$ is the air

temperature inside the cargo area, and $\vartheta_{W1,2} \in \mathbb{R}$ are the temperatures of the wall layers. The control input vector $\boldsymbol{u} = [n_{\mathrm{cpr}}, n_{\mathrm{pump}}]^{\mathrm{T}} \in \mathbb{R}^2_{\geq 0}$ consists of n_{cpr} the compressor speed and n_{pump} the pump speed.

Constant and known parameters are mass $m_{\mathrm{air}} \in \mathbb{R}$ and specific heat of air $c_{p,\mathrm{air}} \in \mathbb{R}$ inside the ICB, heat transfer coefficient $\alpha \in \mathbb{R}$ and wall surface of the ICB $A_{\mathrm{icb}} \in \mathbb{R}_{\geq 0}$, and mass flow $\dot{m}_{\mathrm{gly}} \in \mathbb{R}$ and specific heat $c_{p,\mathrm{gly}} \in \mathbb{R}$ of water–glycol mix. The external heat load is P_{load}, and $\dot{Q}_{\mathrm{eva}}$ and $\dot{Q}_0 \in \mathbb{R}$ are the heat flows of the evaporator and air chiller, respectively. The effect of the pump is modeled by temperature $\vartheta_{\mathrm{eva}}^{in} \in \mathbb{R}$ in (1):

$$\vartheta_{\mathrm{eva}}^{\mathrm{in}} = \frac{1}{\dot{m}_{\mathrm{gly}} c_{p,\mathrm{gly}}} \left(P_{\mathrm{pump}} - \frac{1}{\rho_{\mathrm{gly}}} \Delta p_{\mathrm{pump}} \dot{m}_{\mathrm{gly}} \right) + \vartheta_{\mathrm{gly}}^{\mathrm{out}} \tag{8}$$

where $P_{\mathrm{pump}} \in \mathbb{R}_{\geq 0}$ is the power of the pump, $\rho_{\mathrm{gly}} \in \mathbb{R}$ the density of the water–glycol mixture and Δp_{pump} is the pressure difference of the pump. $\dot{m}_{\mathrm{gly}}$ is defined by

$$\dot{m}_{\mathrm{gly}} = \gamma_1 + \gamma_2 n_{\mathrm{pump}} + \gamma_3 \vartheta_{\mathrm{gly}}^{\mathrm{out}} + \gamma_4 n_{\mathrm{pump}}^2 + \gamma_5 \vartheta_{\mathrm{gly}}^{\mathrm{out}} n_{\mathrm{pump}}.$$

P_{pump} and Δp_{pump} are modeled by the mass flow $\dot{m}_{\mathrm{gly}}$:

$$P_{\mathrm{pump}} = \gamma_6 \dot{m}_{\mathrm{gly}}^2 + \gamma_7 \dot{m}_{\mathrm{gly}} + \gamma_8 \tag{9}$$

$$\Delta p_{\mathrm{pump}} = \gamma_9 \dot{m}_{\mathrm{gly}}^2 + \gamma_{10} \dot{m}_{\mathrm{gly}} + \gamma_{11} \tag{10}$$

The liquid/liquid heat transfer in the evaporator shows a more direct heat transfer than the liquid/gas heat transfer in the air chiller. Assuming a static relation, as shown in [27], the dynamic behavior of the evaporator will be neglected, and the heat flow $\dot{Q}_{\mathrm{eva}}$ of the evaporator is modeled by linear regression:

$$\dot{Q}_{\mathrm{eva}} = \kappa_5 n_{\mathrm{cpr}} \left(\zeta_1 n_{\mathrm{cpr}} - \zeta_2 + \zeta_3 \vartheta_{\mathrm{amb}} + \zeta_4 \vartheta_{\mathrm{gly}}^{\mathrm{out}} \right) \tag{11}$$

The air chiller is modeled as a cross-flow heat exchanger, in accordance with the number of transfer units (NTU) method [30], where $W_{\mathrm{gly}} \in \mathbb{R}$ is the thermal capacity flow of the refrigerant and $e_{\mathrm{gly}} \in \mathbb{R}$ is the operating characteristic. The heat flow of the air chiller is described as

$$\dot{Q}_0 = -\left(\vartheta_{\mathrm{gly}}^{\mathrm{in}} - \vartheta_{\mathrm{air}}^{\mathrm{in}} \right) W_{\mathrm{gly}} e_{\mathrm{gly}}, \tag{12}$$

where

$$e_{\mathrm{gly}} = 1 - \exp\left(\frac{\exp(-C_{\mathrm{gly}} \cdot N_{\mathrm{gly}}) - 1}{C_{\mathrm{gly}}} \right) \tag{13}$$

$$C_{\mathrm{gly,air}} = \frac{W_{\mathrm{gly}}}{W_{\mathrm{air}}} \tag{14}$$

$$N_{\mathrm{gly}} = k_{\mathrm{gly}} \frac{A_{\mathrm{chil}}}{W_{\mathrm{gly}}} \tag{15}$$

$$W_{\mathrm{gly}} = \dot{m}_{\mathrm{gly}} \cdot c_{p,\mathrm{gly}} \tag{16}$$

$$W_{\mathrm{air}} = \dot{m}_{\mathrm{air}} \cdot c_{p,\mathrm{air}}. \tag{17}$$

$W_{\mathrm{air}} \in \mathbb{R}$ is the thermal capacity flow of the air, $C_{\mathrm{gly}} \in \mathbb{R}$ is the ratio of the thermal capacity flows of refrigerant and air, N_{gly} is the referenced transmission capability of the NTU method, $k_{\mathrm{gly}} \in \mathbb{R}$ is the heat transfer coefficient, and $A_{\mathrm{chil}} \in \mathbb{R}$ is the surface of the air chiller.

The unknown parameters in Eqs. (1)–(11) are collected in the parameter vector $\theta \in \mathbb{R}^{28}_{\geq 0}$:

$$\theta = \begin{bmatrix} \beta_{1,\ldots,4} & \gamma_{1,\ldots,11} & \kappa_{1,\ldots,5} & \tau_{1,\ldots,4} & \zeta_{1,\ldots,4} \end{bmatrix}^{\mathrm{T}} \tag{18}$$

A formal discrete-time state space formulation of the model is given by

$$\boldsymbol{x}_{k+1} = \boldsymbol{f}\left(\boldsymbol{x}_k, \boldsymbol{u}_k, \boldsymbol{v}_k, \theta \right) \tag{19}$$

$$\boldsymbol{y}_k = \boldsymbol{x}_k + \boldsymbol{e}_k. \tag{20}$$

The index $k \in \mathbb{N}$ denotes the current time step with a sample time of $T_s = 10\,\mathrm{s}$, and the state vector contains seven temperatures

$$\boldsymbol{x}_k = \begin{bmatrix} \vartheta_{\mathrm{gly}}^{\mathrm{in}} & \vartheta_{\mathrm{gly}}^{\mathrm{out}} & \vartheta_{\mathrm{air}}^{\mathrm{in}} & \vartheta_{\mathrm{air}}^{\mathrm{out}} & \vartheta_{\mathrm{icb}} & \vartheta_{W1} & \vartheta_{W2} \end{bmatrix}^{\mathrm{T}}.$$

$\boldsymbol{u}_k \in \mathbb{R}^2$ is the input vector, and $\boldsymbol{v}_k \in \mathbb{R}^2$ is the measurable disturbance of ambient air temperature and external heat load $\boldsymbol{v}_k = [\vartheta_{\mathrm{amb}} \ P_{\mathrm{load}}]^{\mathrm{T}}$. $\boldsymbol{y}_k \in \mathbb{R}^7$ is the output vector, and $\boldsymbol{e}_k \in \mathbb{R}^7$ are uncorrelated disturbance signals.

4. Model parametrization and validation

The FDI methods utilized here are based on a reliable model. Using measured data from different experiments the initially unknown parameters in θ are determined.

4.1. Model parametrization

Using the set of input/output data, the aim is to determine the parameter vector that minimizes the criterion

$$J_{\theta} = \sum_{k=1}^{N_{\mathcal{I}}} \varepsilon_{\theta,k}^{\mathrm{T}} \Lambda_k^{-1} \varepsilon_{\theta,k} \in \mathbb{R}_{\geq 0}, \tag{21}$$

where $N_{\mathcal{I}} \in \mathbb{N}$ is the number of samples in the identification data set, $\varepsilon \in \mathbb{R}^7$ denotes the prediction error and $\Lambda \in \mathbb{R}^{7 \times 7}_{\geq 0}$ is a diagonal weighting matrix. The prediction error is defined as

$$\varepsilon_{\theta,k} = \boldsymbol{y}_k - \hat{\boldsymbol{y}}_{\theta,k}, \tag{22}$$

where $\hat{\boldsymbol{y}}_{\theta,k} \in \mathbb{R}^7$ is the model's prediction of $\boldsymbol{y}_k \in \mathbb{R}^7$. In order to estimate θ, the prediction error is minimized [31]:

$$\theta^* = \arg\min J_{\theta} \tag{23}$$
$$\text{s.t.}$$
$$0 \leq \theta_i \leq \theta_i^{\mathrm{ub}}, \qquad i \in \{1, \ldots, 27\}$$

Values of $\theta_6^{\mathrm{ub}} = 2.10^4$ and $\theta_i^{\mathrm{ub}} = 2.10^1$ otherwise guarantee good convergence to the optimal solution. The minimization of Eq. (23) is performed by a non-linear least squares algorithm (see [32]). Model validation is shown in Section 4.2 and numerical parameter values can be found in the Appendix (see Table A.3).

4.2. Model validation

To provide an absolute and a relative measure of the model fitness, the RMSE (root mean squared error)

$$\mathrm{RMSE} := \sqrt{\frac{\sum_{i=1}^{N_{\mathcal{V}}} \left(\boldsymbol{y}_i - \hat{\boldsymbol{y}}_i \right)^2}{N_{\mathcal{V}}}} \tag{24}$$

and the fit shown in percentage is based on the normalized root mean squared error (NRMSE)

$$\mathrm{NRMSE} := 1 - \sqrt{\frac{\sum_{i=1}^{N_{\mathcal{V}}} \left(\boldsymbol{y}_{\mathrm{ref},i} - \hat{\boldsymbol{y}}_i \right)^2}{\sum_{i=1}^{N_{\mathcal{V}}} \left(\boldsymbol{y}_{\mathrm{ref},i} - \bar{\boldsymbol{y}}_{\mathrm{ref},i} \right)^2}} \tag{25}$$

are computed, where $N_{\mathcal{V}} \in \mathbb{N}$ is the number of samples in the cross-validation data set, $\boldsymbol{y}_{\mathrm{ref}} \in \mathbb{R}$ is the measured reference data, $\hat{\boldsymbol{y}} \in \mathbb{R}$ is the estimated output, and $\bar{\boldsymbol{y}}_{\mathrm{ref}} \in \mathbb{R}$ is the reference mean.

The cross-validation of the model is shown in Fig. 2. In the top plot, the temperatures of the cooling system are shown (solid-measured, dashed-simulated). In the bottom plot, the residual is almost always within 1 °C; a residual smaller than 2 °C results only for large deviations from the operating point. The model fit based on NRMSE is always above 89% for the validation data set.

The prediction errors remain within an acceptable region around the predicted temperature values, being sufficient for modeling the FDI system. For a detailed discussion of the parameter identification see [26,32].
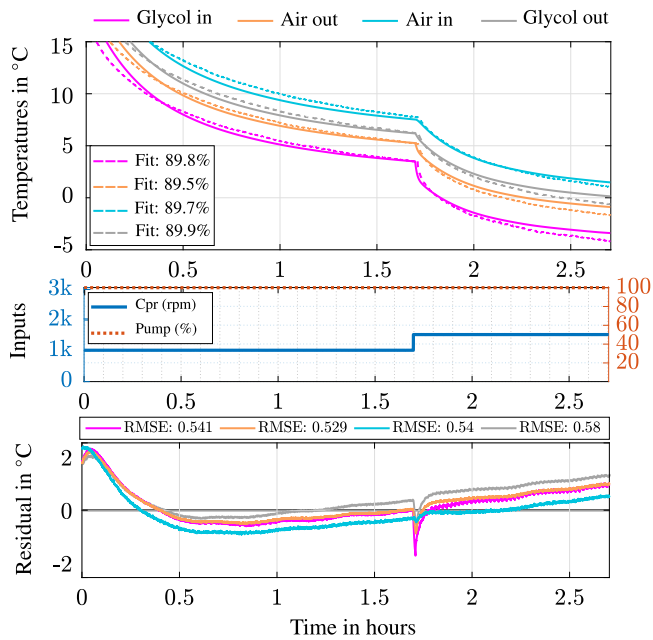
Fig. 2. Top: The validation data set of the gray-box model. Middle: Input signals compressor and pump. Bottom: Residuals in °C and RMSE values.

5. Fault detection and isolation

A model-based FDI design for the secondary loop RS from Section 3 is presented. The structure of the FDI system is based on a detection and isolation layer [14,15]. Both parametric and sensor faults can be detected and isolated, and the selection of thresholds is presented.

5.1. FDI architecture

The FDI structure is shown in Fig. 3. The FDI system is connected in parallel to the plant and its control loop. Fault detection is conducted using the unknown input observer (UIO, residual $r^d \in \mathbb{R}_{\geq 0}$). Fault isolation for parametric faults is achieved by a bank of UIOs (residuals $r^p \in \mathbb{R}_{\geq 0}$), where each model corresponds to one specific fault. The isolation of sensor faults is accomplished by a bank of extended Kalman filters (EKF, residuals $r^s \in \mathbb{R}$) [33]. The index j denotes the specific parametric fault, where $j \in \{1, 2\}$. The index $l \in \{1, 2, \ldots, 4\}$ defines the specific sensor fault. The fault isolation logic that assigns the fault identifier is explained in Section 5.4.

5.2. Unknown input observer

UIOs are used to detect a fault and to isolate the parametric faults of icing/fouling and pump faults. This section reviews general notions about UIO-based estimation and faults isolation (see [14,17] for details). For the observer design the system (19) is linearized around the nominal operating point x_0, u_0:

$$A = \left.\frac{\partial f(t)}{\partial x}\right|_{x_0, u_0} \qquad B = \left.\frac{\partial f(t)}{\partial u}\right|_{x_0, u_0}$$
$$C = \left.\frac{\partial h(t)}{\partial x}\right|_{x_0, u_0} \qquad E = \left.\frac{\partial f(t)}{\partial z}\right|_{x_0, u_0} \qquad (26)$$

where A and B are system and input matrix. C is the output matrix and E is the input vector of the non-measurable input. The design of the UIO is based on the linearized system, where uncertainties are modeled as additive disturbances. The UIO is defined as:

$$z_{k+1} = F z_k + T B u_k + K_{\text{UIO}} y_k \qquad (27)$$
$$\hat{x}_k = z_k + H y_k \qquad (28)$$

where $z_k \in \mathbb{R}$ is the UIO state, $\hat{x}_k$ is the estimate of x_k. The term $K_{\text{UIO}} y_k$ covers additive disturbances or model uncertainties that are not known a priori. Matrices H, T, F, K_{UIO} are defined by

$$H = E\left[(CE)^T(CE)\right]^{-1}(CE)^T \qquad (29)$$
$$A_1 = A - H C A \qquad (30)$$
$$T = I - H C \qquad (31)$$
$$F = A_1 - K_1 C \qquad (32)$$
$$K_{\text{UIO}} = K_1 + F H \qquad (33)$$

The gain matrix K_1 is used for the design of the UIO. The UIO exists (see [14]) if the condition $\text{rank}(CE) = \text{rank}(E)$ holds. Furthermore, matrices (A_1, C) must be a detectable pair.

Utilizing (29) to (33), the state estimation error for all UIOs is $e^i_{k+1} = F e^i_k \in \mathbb{R}$, where $e^i_k = x^i_k - \hat{x}^i_k$ ($i \in \{d, p\}$ for detection and parametric faults, respectively), will asymptotically approach zero if F is positive definite. The associated residual $r^i_k \in \mathbb{R}_{\geq 0}$ is defined as

$$r^i_k = e^{i}_k{}^T \cdot e^i_k. \qquad (34)$$

The residual r^i_k is compared with a threshold $\delta^i \in \mathbb{R}_{\geq 0}$ for detection purposes. An optimal choice for the thresholds under different operating conditions is shown in Section 5.5.

5.3. Extended Kalman filter

Sensor faults for four sensors are covered by the multiple-model EKF-based method. The EKF is an optimal state estimator, which is applied to stochastic dynamic systems. The EKF is a generalization of the KF for a nonlinear system, in which the system is linearized around the last estimation. The system (19) is iterative linearized around the current state vector x_k:

$$A_k = \left.\frac{\partial f(t)}{\partial x}\right|_{\hat{x}_k, u_k}, \qquad B_k = \left.\frac{\partial f(t)}{\partial u}\right|_{\hat{x}_k, u_k}, \qquad C_k = \left.\frac{\partial h(t)}{\partial x}\right|_{\hat{x}_k, u_k}$$

The nonlinear model is used to compute the future state x^-_{k+1} and the current state covariance matrix P^-_k with the following definitions:

$$x^-_{k+1} = f(\hat{x}_k, u_k) \qquad (35)$$
$$P^-_k = A_k \cdot P_{k-1} \cdot A_k^T + Q_k \qquad (36)$$

where $\hat{x}$ is the posterior estimate, $\hat{x}^-_k$ the prior estimate and P_k the state variance matrix. At the correction state, using x^-_k and P^-_k, the Kalman gain $K_{\text{EKF},k}$, and measurement innovation S_k, the update of the error covariance matrix P_k is obtained.

$$S_k = C_k \cdot \hat{P}^-_k \cdot C_k^T + R_k \qquad (37)$$
$$K_{\text{EKF},k} = P^-_k \cdot C_k^T \cdot (C_k \cdot \hat{P}^-_k \cdot C_k^T + R_k)^{-1} \qquad (38)$$
$$P_k = (I - K_k \cdot C_k) P^-_k \qquad (39)$$

The result is an update of the difference between the measured and estimated output.

$$e_k = y_k - C_k \hat{x}^-_k \qquad (40)$$

where y_k is the current measurement. Using Eq. (40) the update of the posterior state estimate is computed:

$$\hat{x}_k = \hat{x}^-_k + K_{\text{EKF},k} \cdot e_k \qquad (41)$$

The a posteriori estimate of the state $\hat{x}_k$ corrects the predicted estimate by including the measurements. Finally, the residual is generated as follows:

$$r^s_k = r_k^T \cdot S_k^{-1} \cdot r_k \qquad (42)$$

Eqs. (35) to (42) are executed recursively for each sensor that is monitored in the FDI algorithm. Residuals of the EKF-bank are generated and collected in a cumulative sum till they exceed a threshold.
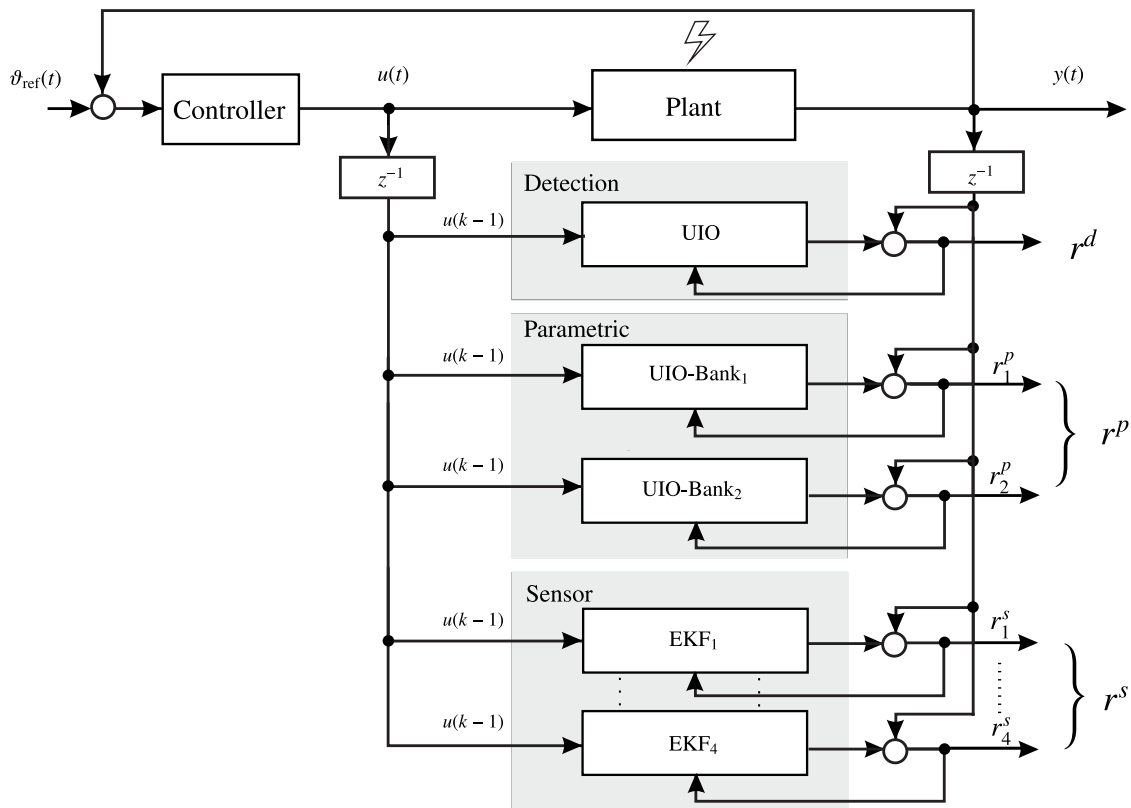
Fig. 3. Block-diagram of interconnections of plant, controller and the proposed method for FDI.
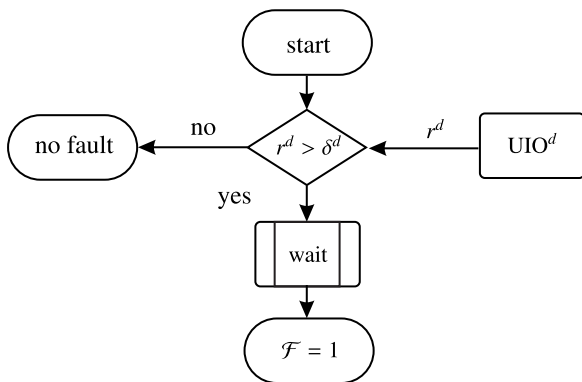

Fig. 4. Flow diagram of the top level fault detection logic.

5.4. Fault isolation logic

The purpose of the fault isolation logic is to specify which fault has occurred based on the transgression of thresholds by the residuals.

On the top level, fault detection for all faults is achieved by the detection UIO (see Fig. 3). A fault is detected if the residual r^d of the detection UIO is greater than the pre-defined threshold $\delta^d \in \mathbb{R}_{\geq 0}$, Fig. 4. To avoid toggling, a waiting time t_{wait}=120 s is defined. t_{wait} is the minimum time that the detection condition has to be continuously met before it is detected which is indicated by $\mathcal{F} \in \{0, 1\}$.

On a lower level, fault isolation is achieved for parametric faults and sensor faults by the logic shown in Fig. 5. The residuals for parametric faults r^p (from the UIOs) and sensor faults r^s (from the EKFs) are analyzed. Both residuals are processed in an analogous way: First, the residuals are compared to suitable thresholds δ^p and δ^s (see Section 5.5 for threshold selection). For each active fault, a counter $\chi^{p,s} \in \mathbb{N}$ is

incremented until all residuals have been checked. If no threshold is exceeded, no fault is detected in spite of the positive detection UIO.

Using the counter values, a check for a unique fault identification is conducted. Simultaneous faults ($\chi^{p,s} > 1$) lead to the classification "unknown fault". If only one of the residuals exceeds the threshold, a unique fault ID is assigned after a holding time of $1000\,\text{s}$.

5.5. Selection of thresholds

In order to obtain valid thresholds, stationary values of the residuals for fault-free operation are evaluated over the complete operating range. The thresholds are then selected such that no false alarms occur in stationary operation.

Fig. 6 shows the values of the residuals in stationary operation for the different observers. The colored surfaces (blue to yellow) show the values of the respective residuals, while the red surfaces show suitable threshold values.

Fig. 6(a) shows that the threshold of the detection observer is constant at 4000. In nominal operating mode, the residuals are below the threshold and no false alarm is triggered. Fig. 6(b) shows the residual values and threshold for the parametric air chiller fault. In this case, a fault would be triggered if the residual ends up below the red threshold area. The threshold value was therefore set to a constant of 1500. In Fig. 6(c) the threshold for the parametric pump fault was set to a constant value of 25000 and intersects the surface of the Residual in one corner. This is justified by the fact that no operation occurs in that area.

In Fig. 6(d) the residual values for one of the Kalman filters are shown. An admissible band is defined by two parallel red surfaces. Note that for each of the four different Kalman filters (see Fig. 3) such a surface has been defined. The following equation shows the definition of one threshold function:

$$\delta^s = \phi_1 + \phi_2\, n_{\text{cpr}} + \phi_3\, \vartheta_{\text{amb}} + \phi_4\, n_{\text{cpr}}^2 + \phi_5\, n_{\text{cpr}}\, \vartheta_{\text{amb}} + \phi_6\, \vartheta_{\text{amb}}^2 \qquad (43)$$
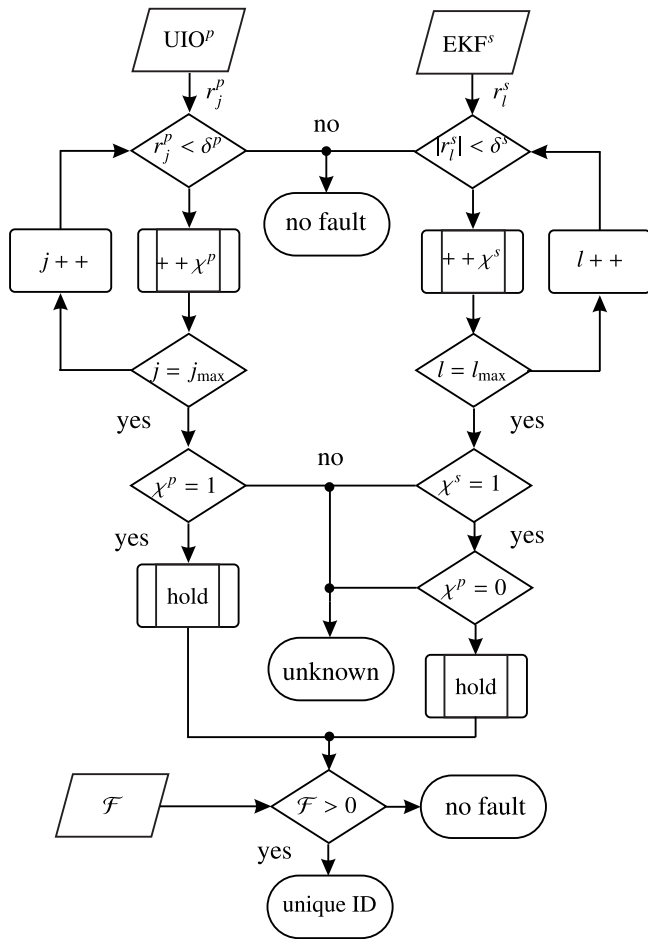
Fig. 5. Flow-diagram of the lower level fault isolation.

where n_{cpr}, ϑ_{amb} are the time varying variables and $\phi_{1,\ldots,6} \in \mathbb{R}$ are the constants of the threshold function $\delta^s \in \mathbb{R}$.

6. Laboratory setup

Fig. 7 shows the test bench where the FDI algorithm was implemented and tested. The complete test bench is located in a temperature-controlled chamber with circulating airflow and stable ambient temperature. The ambient temperature was constant $\vartheta_{amb} = 25.0$ °C during all test scenarios.

As shown in Fig. 7, the cooling system consists of an outer and an inner unit. The wooden box also called a calorimeter box, is insulated with extruded styrofoam and has similar dimensions and thermal characteristics to the cool box of a delivery vehicle [26]. The complete data acquisition system is presented in [27].

The air chiller inside the box is equipped with a flap (see Fig. 7) (a) partly covering the air path of the chiller when closed. This flap can be actuated from the outside and emulates icing or fouling when closed. Also, a camera is mounted in front of the air-chiller outlet to monitor the icing and correct closing of the flap. The sensors for the glycol temperature ϑ_{gly}^{in} and ϑ_{gly}^{out} are located in the inner unit near the air-chiller, as shown in Fig. 7(a). The sensors for the air-flow temperature ϑ_{air}^{in} and ϑ_{air}^{out} are located in front of and behind the air-chiller. The

standard deviation of the implemented DS18S20 sensors are ± 0.5 °C over the range -55 °C to $+125$ °C, compare [34].

A heating load P_{load} is placed inside the box to emulate time-varying heat loads such as ambient temperature or irradiation. During the test scenarios, the load is held constant at $P_{load} = 300\ W$. Additionally, vapor can be inserted into the box through the same opening used for cables and sensors to emulate the effect of door openings in humid ambient air conditions (see Fig. 7(b)).

7. Test conditions for faults

Experimental measurement data (total length: 21.4 h) obtained from the test bench were gathered to demonstrate the FDI performance. The following subsections describe the test conditions during fault-free and faulty operation, where parametric and sensor faults are covered.

7.1. Fault-free operation

For fault-free operation, the system is in nominal condition. The secondary loop pump delivers a constant mass flow of the water–glycol mixture of 8.6 kg/min at $n_{pump} = 100\%$. The compressor speed is constant throughout the whole experiment $n_{cpr} = 1800$rpm. The full surface of the air chiller is available (no ice, metal flap is open). For parametric faults, stationary operation precedes the fault. For sensor faults, a series of steps on the compressor speed is performed to highlight the performance during transient operation.

7.2. Faulty operation

The conditions under which the faults were introduced are described in the following section.

7.2.1. Parametric faults
Icing fault: Two related air chiller faults are considered:

1. Water vapor is fed into the test bench through a duct (compare Fig. 7(a) & (b)). The vapor supply was continued until an expert watching the camera image considered de-icing to be necessary.
2. An articulated flap is closed and covers 30% of the air chiller surface.

The test bench is adapted to emulate both failures, as can be seen in Fig. 7. Both mechanisms can be triggered when the box is closed. The water vapor feed emulates the effect of opening the doors of the ICB, causing warm and humid ambient air to enter and subsequently icing up the air chiller. The flap emulates sudden (partial) blocking of the evaporator surface by payload or dirt.

Pump fault: A fault in the secondary loop pump, e.g. loss of power or wear, can reduce the mass flow of the glycol–water mixture. A power reduction by 50% reduces the mass flow to 3.5 kg/min. A power reduction to 30% causes a mass flow to 2.0 kg/min. To emulate this fault, the power of the water pump is reduced without forwarding the information to the FDI system. All other settings are kept at the nominal operation.

7.3. Sensor faults

The temperature sensor faults considered are drift and offset in both positive and negative directions. Step changes in compressor speed demonstrate the functionality of the FDI during transient operation. For the sensor offset a constant value of ± 3.0 °C is added to the real test bench measurements (six times the standard deviation of the sensor stated by the manufacturer). Sensor drift is realized by a ramp with a slope of ± 0.001 °C/s per sample T_s added to the sensor measurement.
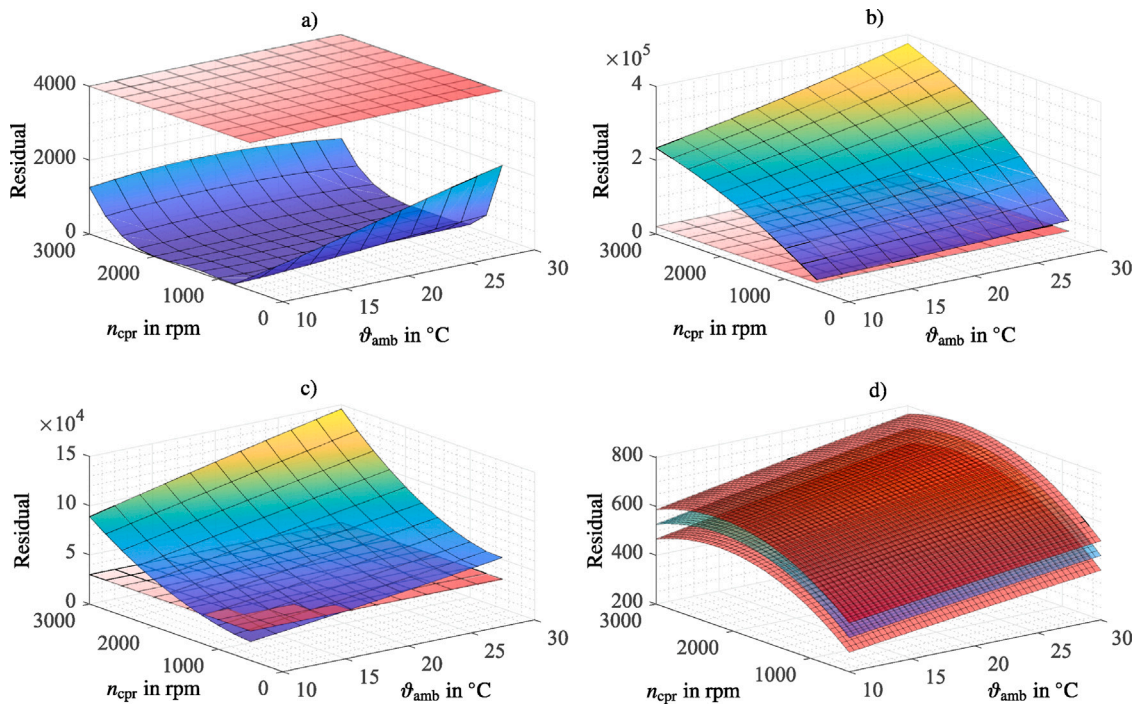
Fig. 6. Plot of stationary residuals (colored surface) and their respective thresholds (red surface). (a): Residual surface Fault Detection (b): Residual surface Parametric Fault: air chiller (c): Residual surface Parametric Fault: pump (d): Residual surface Sensor Fault EKFs.
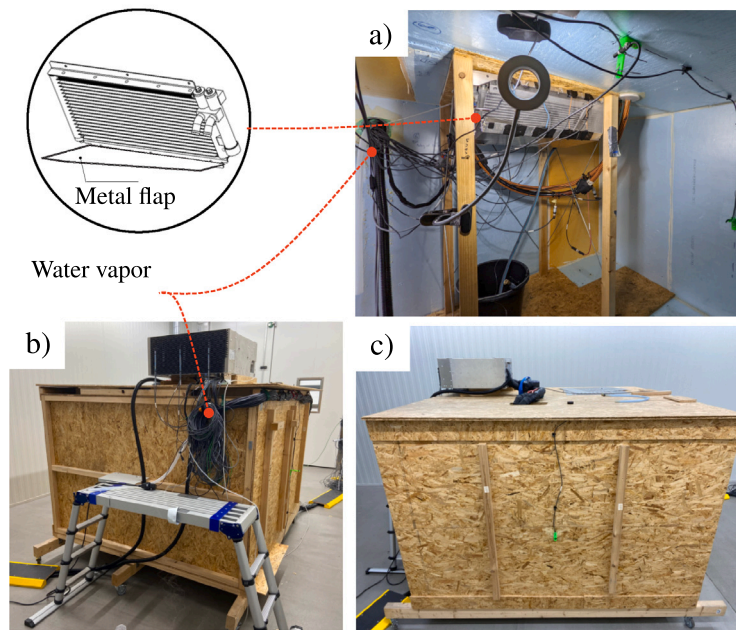

Fig. 7. (a): Images of the prepared inner unit inside the wooden box. (b): Image of the test bench with an outer unit on top and all sensor/tube connections. (c): Image of the side view of the test bench.

7.4. Monte Carlo simulation

To check for reliability a Monte Carlo simulation of 200 runs for each fault type was conducted. Every fault was tested with three different fault levels (FL) to find the average fault detection rate (DR) and false alarm rate (FAR). For parametric faults FL1,2 and 3 indicate reductions of the nominal values by 10, 40, and 70%, respectively. The FLs of the sensor faults refer to a percentage (10, 40, and 70%) of a reference fault value. That reference value is set to ± 4 °C for offset and ± 0.002 °C/s for drift. With increasing FL the severity of the fault increases.

8. Results on fault detection and isolation

In the following section, the results for fault identification and isolation are presented.
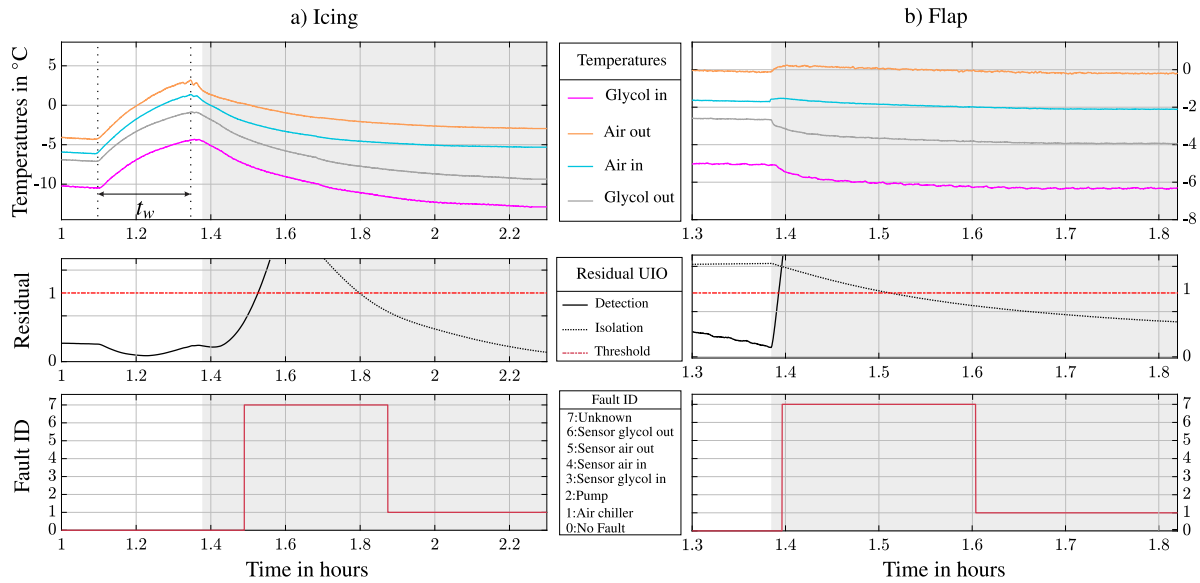
Fig. 8. Icing faults. (a): Water vapor causes icing. (b): Air-chiller obstructed by flap. Top: Temperatures of secondary loop. Middle: Normalized residuals of detection and isolation UIOs, respectively. Bottom: Fault Identifier. Gray areas indicate faulty conditions.

8.1. Icing fault experiments

In the top plot of Fig. 8(a), the fault of icing of the air chiller is shown. Water vapor fed into the cooling chamber with subsequent icing causes temperatures both in the ICB (ϑ_{air}^{out} and ϑ_{air}^{in}) and in the secondary loop (ϑ_{gly}^{out} and ϑ_{gly}^{in}) to rise (time span t_w starting at $t = 1.1$ h). After the shutdown of the feed ($t = 1.32$ h), temperatures drop again and icing begins. The gray area in Fig. 8 shows the time span in which icing on the air-chiller was visible on the camera. The onset of icing is also visible in the detection residual in the middle subplot. The icing fault was detected at $t = 1.5$ h by the detection UIO. The fault isolation residual correctly indicates an air-chiller fault at $t = 1.8$ h after initially delivering an unknown fault (see the bottom plot in Fig. 8(a)), starting at $t = 1.5$ h. Correct isolation is achieved after the holding time t_{hold} (Section 5.4) at $t = 1.85$ h.

Sudden obstruction by a flap shown in Fig. 8(b) occurs at $t = 1.38$ h. As shown in the top plot of Fig. 8(b) the temperatures of ϑ_{gly}^{out} and ϑ_{gly}^{in} decrease due to a reduced effective temperature coefficient.

The detection residual (middle subplot) reacts with a sharp rise. The isolation residual reacts much slower, and correct fault identification is achieved 0.85 h after the obstruction (bottom plot).

8.2. Pump fault experiments

In the top left plot of Fig. 9(a), a fault of 50% reduction of pump power is shown. The fault (gray area) causes the temperatures ϑ_{gly}^{out} and ϑ_{gly}^{in} to react in opposite directions.

In the second subplot of Fig. 9(a), the detection observer (UIO, solid line) indicates the fault at $t = 0.72$ h. The isolation of the fault (UIO, dashed line) starts with the occurrence of the fault. A pump fault is indicated even before the detection has reached the threshold. After the holding time defined in Section 5.4, the fault isolation is correctly completed (see the third subplot of Fig. 9(a)).

In Fig. 9(b), a fault with pump power reduction to 30% is shown. In the top plot of Fig. 9(b), the system response is less pronounced than before. This causes the detection observer to react slower than in the previous scenario. At $t = 0.87$ h the fault is correctly isolated.

Table 1
Sensor fault isolation: results from test bench experiments.

Fault scenarios	ϑ_{gly}^{out}	ϑ_{air}^{in}	ϑ_{air}^{out}	ϑ_{gly}^{in}
offset +	✓	✓	✓	✓
offset −	△	✓	✓	✓
drift +	◇	✓	◇	✓
drift −	△	✓	✓	◇

Symbol: ✓: correctly detected; △: first pump, then correct; ◇: first icing, then correct.

8.3. Sensor faults experiments

Each of the four temperature sensors, ϑ_{gly}^{out}, ϑ_{gly}^{in}, ϑ_{air}^{out} and ϑ_{air}^{in} was tested for all fault scenarios. From these results, the negative drift and positive offset fault are shown (see Fig. 10). Sensor drift on ϑ_{air}^{out} is shown on the left of Fig. 10(a), and a sudden sensor offset on ϑ_{gly}^{out} on the right of Fig. 10(b).

Fault detection for the sensor drift takes longer, as shown in Fig. 10(a). After the actual fault at $t = 3.7$ h, the first (false) classification is obtained at $t = 5.3$ h. The final correct classification is only achieved at t=6 h after a fault duration of 2.3 h. As shown in Fig. 10(b), the detection of the sensor offset is much faster; after 0.2 h a first (unknown) fault is indicated. After another 0.25 h, the correct fault is isolated. The complete results for sensor faults can be found in Table 1.

8.4. Monte Carlo simulation on reliability

Using the model presented in Sections 3 and 4 a Monte Carlo simulation with the faults described in Section 7.4 was performed. For the parametric faults measurement noise was added (standard deviation of 0.05 °C) and the compressor speed was randomly varied for each run with a standard deviation of 200 rpm around the nominal set point (1800 rpm). For sensor faults, the measurements of the test bench were used. In all Monte Carlo, simulations faults were initiated at random locations.

In Table 2 the results are given. All faults can be reliably detected as the DRs and FARs are in the typical range of other reported FDI
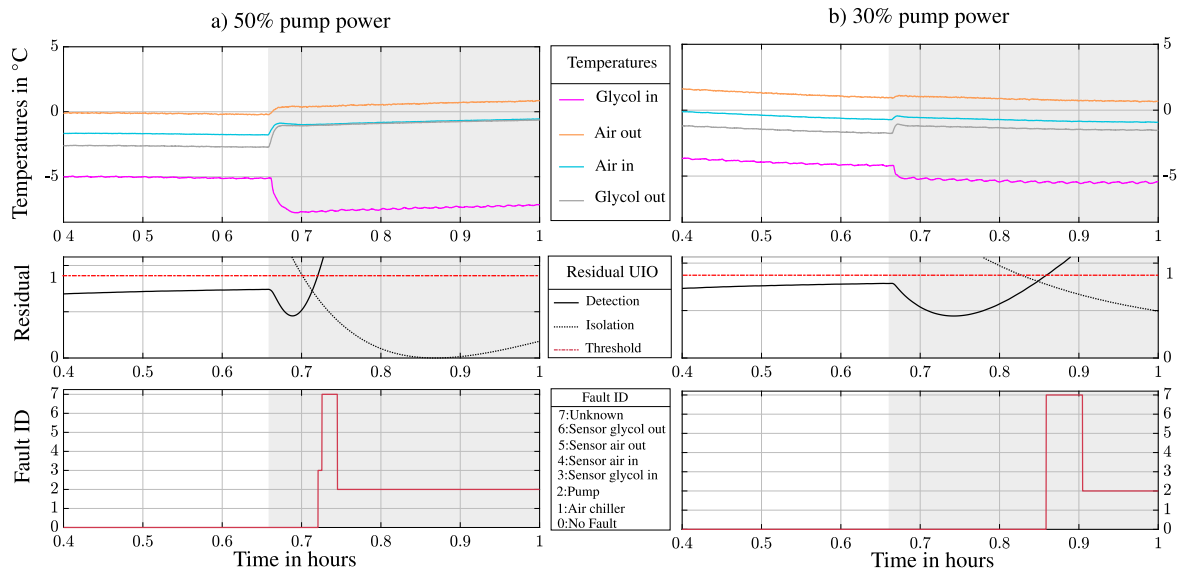
Fig. 9. Pump faults. (a): 50% pump power. (b): 30% pump power. Top: Temperatures of secondary loop. Middle: Normalized residuals of detection and isolation UIOs, respectively. Bottom: Fault Identifier. Gray areas indicate faulty conditions.
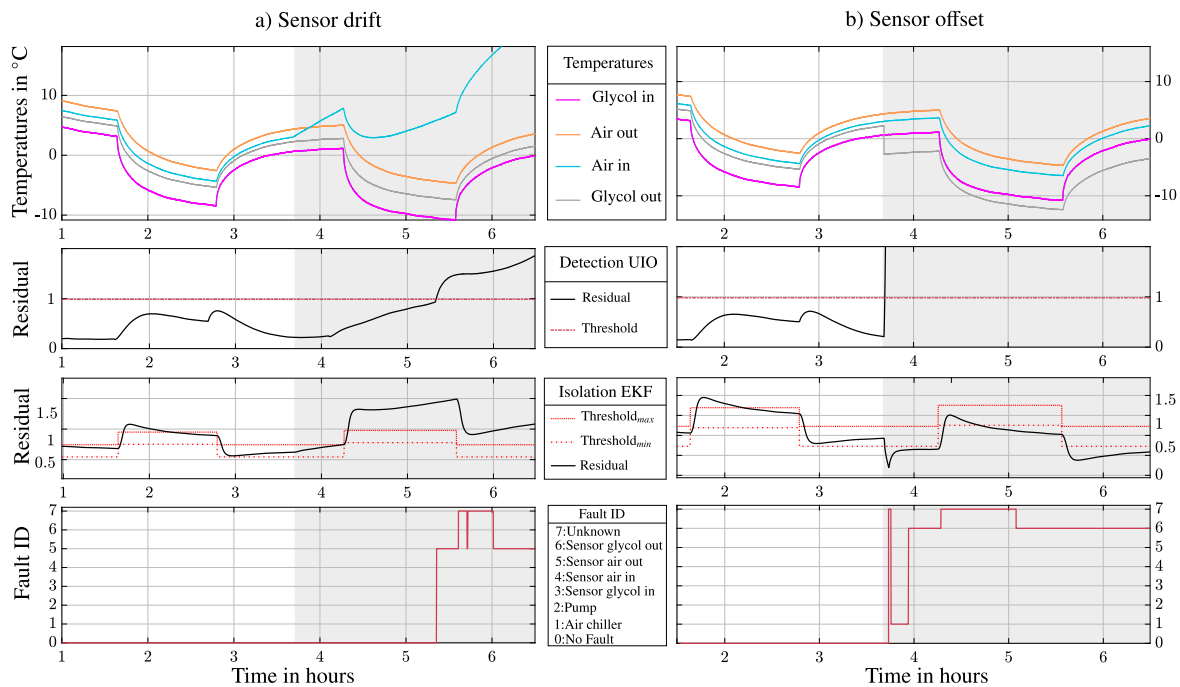

Fig. 10. Sensor faults. (a): Sensor drift. (b) Sensor offset. Top: Temperatures of secondary loop. Second from top: Normalized residual of detection UIO, respectively. Third from top: Residual of isolation UIO. Bottom: Fault Identifier. The gray area indicates faulty conditions.

Table 2
Monte Carlo simulation results for fault detection rate and false alarm rate in %.

Fault level	Icing		Pump		Offset		Drift	
	DR	FAR	DR	FAR	DR	FAR	DR	FAR
FL1	67.3	2.8	78.1	0.2	68.7	3.5	68.6	6.7
FL2	70.5	0.7	79.3	1.5	73.4	2.7	74.9	5.3
FL3	74.9	0	84.3	0.1	77.9	0.9	82.3	2.1
Average	70.9	1.2	80.6	0.6	73.3	2.3	75.3	4.7

implementations. The parametric fault icing shows the smallest FAR rate. The pump fault shows the highest FAR at FL3, similar to the experiments.

Conclusion

This study aimed to find a model-based fault detection and isolation (FDI) system for a secondary loop refrigeration system suitable for detecting both parametric and sensor faults. The key findings are as follows:

Table A.3
Numerical values of measured model parameters.

Parameter	Symbol	Value	Unit
Surface area ICB	A_{icb}	13.57	m^2
Surface air chiller	A_{chil}	0.07	m^2
Surface air chiller flap	A_{flap}	0.023	m^2
Heat load	P_{load}	300	W
Density glycol/water	ρ_{air}	1.04e03	kgm^3
styrofoam thickness	d_{iso}	8.0	cm
Wood panels thickness	d_{wood}	1.2	cm
Heat transfer coefficient	α	0.396	$Wm^{-2}K^{-1}$
Mass air ICB	m_{air}	93.02	kg
Thermal transmittance	k_{gly}	479.59	$Wm^{-2}K^{-1}$
Heat capacity gly/air	$c_{p,gly}$	3.51	$kJkg^{-1}K^{-1}$
Heat capacity air (wet)	$c_{p,air}$	1.08	$kJkg^{-1}K^{-1}$

Table A.4
Numerical values of identified model parameters.

Parameter	Symbol	Value	Unit
Gain glycol in	κ_1	1.012	–
Gain glycol out	κ_2	0.969	–
Gain air in	κ_3	1.065	–
Gain air out	κ_4	0.967	–
Scaling factor	κ_5	1.3e4	rpm^{-1}
Wall model	β_1	6.6e−4	s^{-1}
Wall model	β_2	0.0071	s^{-1}
Wall model	β_3	0.0055	s^{-1}
Wall model	β_4	5.3e−4	s^{-1}
Time const. glycol in	τ_1	17.35	s
Time const. glycol out	τ_2	4.09	s
Time const. air in	τ_3	10.56	s
Time const. air out	τ_4	8.25	s
Pump mass flow	γ_1	0.003	$kg\,s^{-1}$
Pump mass flow	γ_2	0.06	$kg(s\,\%)^{-1}$
Pump mass flow	γ_3	1.1e−5	$kg(s°C)^{-1}$
Pump mass flow	γ_4	2.7e−4	$kg\,(s\,\%^2)^{-1}$
Pump mass flow	γ_5	0.0014	$kg\,(s\%°C)^{-1}$
Pump power	γ_6	0.32	$W\,s^2\,kg^{-2}$
Pump power	γ_7	2.37	$W\,s\,kg^{-1}$
Pump power	γ_8	0.08	W
Pump pressure	γ_9	0.0024	$(m\,kg)^{-1}$
Pump pressure	γ_{10}	0.057	$(m\,s)^{-1}$
Pump pressure	γ_{11}	0.001	$kg(s^2\,m)^{-1}$
Evaporator	ζ_1	2.6e−4	$Wrpm^{-1}$
Evaporator	ζ_2	0.12	W
Evaporator	ζ_3	3.0e−3	$W°C^{-1}$
Evaporator	ζ_4	1.5e−3	$W°C^{-1}$

- A dynamic model of the secondary loop refrigeration system can be built with reasonable effort using first principles. A compact set of experimental data suffices to obtain a good model fit.
- Both sensor and parametric faults in the secondary loop can be reliably detected by the proposed FDI structure.
- The performance of the secondary loop FDI system is in line with the published results for the conventional system and was demonstrated by experimental results.

The findings demonstrate that parametric faults in the secondary loop of the RS are detectable and can be isolated from each other and sensor faults. Parametric faults are quickly and reliably detected, while sensor faults show a longer time delay for detection. All delays are still reasonable in practical applications to prevent prolonged operations with faulty measurements.

Some sensor faults, e.g. ϑ_{gly}^{out}, are more challenging to isolate than others (see Table 1). This is caused by the similar dynamics of parametric faults but also by the preference of parametric fault detection over sensor fault detection. Different design parameters could shift this balance in favor of sensor faults. Since all sensor faults can be isolated correctly, the temporary false classification is considered acceptable.

The model-based approach intrinsically covers the nonlinearities of the system. Correct dynamics over the whole operation are obtained using both unknown input observers and extended Kalman filters. The parametrization of the thresholds in Section 5.5 reflects that fact: Due to the nonlinear characteristic of the surfaces, the thresholds are adapted to the complete operating range.

More advanced FDI formulations are available, especially in the area of data-driven algorithms. These algorithms often outperform model-based formulations. However, for small units and low system complexity, this advantage disappears [11]. On the downside, these data-driven methods rely on the availability of sufficiently large data sets, which may not be available during the design phase.

Moreover, a steady-state detector, as required by the majority of FDI methods, is not needed; the proposed approach works for transient as well as steady-state operation in the complete operating region.

One of the limitations of the presented FDI method is that it cannot isolate simultaneous faults. The presented approach is still able to detect the presence of simultaneous faults quickly but will indicate an unknown fault. Although multiple model-based methods can overcome this problem, they are considerably more complex and require more modeling effort.

Another problem is the limited scalability of the approach: If the RS becomes more complex, the model will have more internal states, include more parameters, and thus the identifiability of the parameters will deteriorate.

A necessary prerequisite for the practical implementation of the method is the use of a climatic chamber to obtain well-defined ambient conditions. Only then will a compact data set be adequate for parameter estimation without systematic errors. Another requirement is the availability of a capable computing unit as small refrigeration systems are often controlled by simple micro-processors.

The economic impact of any reliable FDI is closely connected to the choice of the threshold values. Although a systematic way to select these values has been outlined in this study, and a Monte Carlo simulation demonstrates the reliability of the system, a strong dependence on the application area will remain. Exclusively application-specific measurement data could be the basis for further investigation.

Further work includes a statistical evaluation and optimization of the thresholds and the associated time delays based on real-world data. Another task of interest is the comparative implementation of a more advanced FDI method, e.g. feature engineering or Bayesian networks.

Declaration of competing interest

The authors declare that they have no known competing financial interests or personal relationships that could have appeared to influence the work reported in this paper.

Data availability

The data that has been used is confidential.

Appendix. Parameters of the model

In Table A.3 the parameters that were measured and in Table A.4 the parameters that were identified for the model are shown.

References

[1] S. James, C. James, J. Evans, Modelling of food transportation systems – a review, Int. J. Refrig. 29 (6) (2006) 947–957, http://dx.doi.org/10.1016/j.ijrefrig.2006.03.017, Issue with Special Emphasis on Data and Models on Food Refrigeration.

[2] S. Tassou, G. De-Lille, Y. Ge, Food transport refrigeration – Approaches to reduce energy consumption and environmental impacts of road transport, Appl. Therm. Eng. 29 (8) (2009) 1467–1477, http://dx.doi.org/10.1016/j.applthermaleng.2008.06.027.

[3] A. Rogers, F. Guo, B. Rasmussen, A review of fault detection and diagnosis methods for residential air conditioning systems, Build. Environ. 161 (2019) 106236, http://dx.doi.org/10.1016/j.buildenv.2019.106236.

[4] M.R. Brambley, P. Haves, S.C. McDonald, P. Torcellini, D. Hansen, D. Holmberg, K.W. Roth, Advanced Sensors and Controls for Building Applications: Market Assessment and Potential R&D Pathways, Report PNNL-15149, Pacific Northwest National Laboratory, Washington, DC, USA, 2005, http://dx.doi.org/10.1016/j.enbuild.2020.110492.

[5] H.V. Inamdar, E.A. Groll, J.A. Weibel, S.V. Garimella, Prediction of air-side particulate fouling of HVAC&R heat exchangers, Appl. Therm. Eng. 104 (2016) 720–733, http://dx.doi.org/10.1016/j.applthermaleng.2016.05.082.

[6] B.A. Qureshi, S.M. Zubair, The impact of fouling on the condenser of a vapor compression refrigeration system: An experimental observation, Int. J. Refrig. 38 (2014) 260–266, http://dx.doi.org/10.1016/j.ijrefrig.2013.08.012.

[7] Y. Yu, D. Woradechjumroen, D. Yu, A review of fault detection and diagnosis methodologies on air-handling units, Energy Build. 82 (2014) 550–562, http://dx.doi.org/10.1016/j.enbuild.2014.06.042.

[8] C.G. Mattera, J. Quevedo, T. Escobet, H.R. Shaker, M. Jradi, A method for fault detection and diagnostics in ventilation units using virtual sensors, Sensors 18 (11) (2018) 3931, http://dx.doi.org/10.3390/s18113931.

[9] M.S. Mirnaghi, F. Haghighat, Fault detection and diagnosis of large-scale HVAC systems in buildings using data-driven methods: A comprehensive review, Energy Build. 229 (2020) 110492, http://dx.doi.org/10.1016/j.enbuild.2020.110492.

[10] A comparison study of basic data-driven fault diagnosis methods for variable refrigerant flow system, Energy Build. 224 (2020) 110232, http://dx.doi.org/10.1016/j.enbuild.2020.110232.

[11] G. Li, Y. Hu, J. Liu, X. Fang, J. Kang, Review on fault detection and diagnosis feature engineering in building heating, ventilation, air conditioning and refrigeration systems, IEEE Access 9 (2020) 2153–2187, http://dx.doi.org/10.1109/ACCESS.2020.3040980.

[12] A. Behfar, D. Yuill, Y. Yu, Automated fault detection and diagnosis methods for supermarket equipment (RP-1615), Sci. Technol. Built Environ. 23 (8) (2017) 1253–1266, http://dx.doi.org/10.1080/23744731.2017.1333352.

[13] J. Zhang, A.K. Swain, S.K. Nguang, Robust Observer-Based Fault Diagnosis for Nonlinear Systems using MATLAB®, Springer, 2016, http://dx.doi.org/10.1007/978-3-319-32324-4.

[14] Z. Yang, K.B. Rasmussen, A.T. Kieu, R. Izadi-Zamanabadi, Fault detection and isolation for a supermarket refrigeration system–part one: Kalman-filter-based methods, IFAC Proc. Vol. 44 (1) (2011) 13233–13238, http://dx.doi.org/10.3182/20110828-6-IT-1002.03115.

[15] Z. Yang, K.B. Rasmussen, A.T. Kieu, R. Izadi-Zamanabadi, Fault detection and isolation for a supermarket refrigeration system–Part two: Unknown-input-observer method and its extension, IFAC Proc. Vol. 44 (1) (2011) 4238–4243, http://dx.doi.org/10.3182/20110828-6-IT-1002.03120.

[16] L.F.S. Larsen, R. Izadi-Zamanabadi, R. Wisniewski, Supermarket refrigeration system - Benchmark for hybrid system control, in: 2007 European Control Conference, ECC, IEEE, 2007, pp. 113–120, http://dx.doi.org/10.23919/ECC.2007.7068750.

[17] A.E.O. Hassan, T.A.A. Mohammed, et al., Fault detection in a three tanks hydraulic system using unknown input observer and extended Kalman filter, J. Eng. Res. 9 (4A) (2021) http://dx.doi.org/10.36909/jer.8985.

[18] J. Han, S. Yu, J. Han, Fault detection and isolation for a cooling system of fuel cell via model-based analysis, Processes 8 (9) (2020) 1115, http://dx.doi.org/10.3390/pr8091115.

[19] J. Zarei, E. Shokri, Robust sensor fault detection based on nonlinear unknown input observer, Measurement 48 (2014) 355–367, http://dx.doi.org/10.1016/j.measurement.2013.11.015.

[20] Q. Zhang, M. Canova, Fault detection and isolation of automotive air conditioning systems using first principle models, Control Eng. Pract. 43 (2015) 49–58, http://dx.doi.org/10.1016/j.conengprac.2015.06.005.

[21] Z. Ming, Energy analysis of various supermarket refrigeration systems, in: 11th International Refrigeration and Air Conditioning Conference At Purdue West Lafayette, USA, Paper, Vol. 856, 2006, https://docs.lib.purdue.edu/iracc/856/.

[22] K. Wang, M. Eisele, Y. Hwang, R. Radermacher, Review of secondary loop refrigeration systems, Int. J. Refrig. 33 (2) (2010) 212–234, http://dx.doi.org/10.1016/j.ijrefrig.2009.09.018.

[23] G.S. Kazachki, D.K. Hinde, Secondary coolant systems for supermarkets, ASHRAE J. 48 (9) (2006) 34–47.

[24] W.-B. Yi, K.-H. Choi, J.-I. Yoon, C.-H. Son, S.-J. Ha, M.-J. Jeon, Exergy characteristics of R404A indirect refrigeration system using CO2 as a secondary refrigerant, Heat Mass Transf. 55 (4) (2019) 1133–1142, http://dx.doi.org/10.1007/s00231-018-2497-x.

[25] F. Hanslik, J. Suess, Water as a refrigerant in centrifugal compressor cooling systems for industrial applications, in: Advanced Cooling Technologies and Applications, IntechOpen, 2018, http://dx.doi.org/10.5772/intechopen.79614.

[26] M. Fallmann, A. Poks, M. Kozek, Hybrid model-based online estimation of air temperature in mobile small-scale cooling chambers, Appl. Therm. Eng. 208 (2022) 118147, http://dx.doi.org/10.1016/j.applthermaleng.2022.118147.

[27] M. Fallmann, A. Poks, M. Kozek, Control-oriented hybrid model of a small-scale refrigerated truck chamber, Appl. Therm. Eng. 220 (2023) 119719, http://dx.doi.org/10.1016/j.applthermaleng.2022.119719.

[28] A. Afram, F. Janabi-Sharifi, Review of modeling methods for HVAC systems, Appl. Therm. Eng. 67 (1–2) (2014) 507–519, http://dx.doi.org/10.1016/j.applthermaleng.2014.03.055.

[29] K.K. Kresten K. Sørensen, M.J. Skovrup, L.M. Jessen, J. Stoustrup, M.J. Skovrup, L.M. Jessen, J. Stoustrup, Modular modeling of a refrigeration container, Int. J. Refrig. 55 (2015) 17–29, http://dx.doi.org/10.1016/j.ijrefrig.2015.03.017.

[30] H.D. Baehr, K. Stephan, Wärme-Und Stoffübertragung, Vol. 7, Springer, 1994, http://dx.doi.org/10.1002/bbpc.199500102.

[31] A. Simpkins, System identification: Theory for the user, (Ljung, L.; 1999), IEEE Robot. Autom. Mag. 19 (2) (2012) 95–96, http://dx.doi.org/10.1109/MRA.2012.2192817.

[32] L. Ljung, R. Singh, Version 8 of the matlab system identification toolbox, IFAC Proc. Vol. 45 (16) (2012) 1826–1831, http://dx.doi.org/10.3182/20120711-3-BE-2027.00061, 16th IFAC Symposium on System Identification.

[33] R. Isermann, Fault-Diagnosis Systems: An Introduction from Fault Detection to Fault Tolerance, Springer Science & Business Media, 2005, http://dx.doi.org/10.1007/978-3-642-12767-0.

[34] otom Group GmbH, Datasheet: Dallas DS18S20. https://www.sensorshop24.de/kabelfuehler-durchmesser-6mm.